Retrieving Ocean Surface Wind Speeds in Real Time on Spaceborne GNSS-R Receivers: Algorithm and Validation

Tongsheng Qiu, Qi Zheng, Xianyi Wang, Feixiong Huang, Junming Xia, Fu Li, Zhuoyan Wang, Yueqiang Sun, Qifei Du, Weihua Bai, Yuerong Cai, Dongwei Wang, Yusen Tian, and Shuangshuang Cheng

***Abstract*—Based on delay-Doppler maps (DDMs) in raw counts generated by spaceborne global navigation satellite system reflectometry (GNSS-R) receivers, retrieving ocean surface wind speeds is feasible, so several spaceborne GNSS-R missions have been carried out. However, it is currently troubled by global data latency of several hours or even more due to the bottleneck in the satellite downlink. Consequently, this article, for the first time, presents an algorithm for spaceborne GNSS-R receivers to conduct the DDM calibration in orbit and then to retrieve ocean surface wind speeds in real time, which contributes to not only lightening the burden on downloading a wealth of scientific data but also broadcasting real-time ocean surface wind speeds to users. Since there is a power correlation between direct and reflected signals from the same GNSS satellite with respect to the GNSS-R receiver, this algorithm calibrates direct signal power first, and then it estimates the real-time GNSS transmitter effective isotropic radiated power at the reflected signal according to the normalized antenna pattern of the corresponding GNSS satellite. Afterward, DDMs in raw counts are calibrated. Finally, ocean surface wind speeds are computed using pretrained geophysical model functions. Exploiting the scientific data from the GNOS-II onboard China's FY-3E satellite, this algorithm is validated carefully, and final retrieved ocean surface wind speeds against collocated European Centre for Medium-Range Weather Forecasts wind speeds have an overall root-mean-square error of 1.68 m/s and 1.50 m/s for GPS-R and BDS-R, respectively.**

***Index Terms*—Algorithm, ocean surface wind speeds, real-time retrieval, spaceborne global navigation satellite system reflectometry (GNSS-R) receiver, validation.**

Manuscript received 31 August 2023; revised 23 November 2023; accepted 15 December 2023. Date of publication 20 December 2023; date of current version 3 January 2024. This work was supported in part by the Feng Yun 3 (FY-3) Global Navigation Satellite System Occultation Sounder Development and Manufacture Project led by NSSC, CAS, in part by the Strategic Priority Research Program of Chinese Academy of Sciences under Grant XDA15012300, in part by the Scientific Research Project of the Chinese Academy of Science under Grant YZ201129, in part by the Youth Innovation Promotion Association, CAS, under Grant 2018180, in part by the Youth Cross Team Scientific Research Project of the Chinese Academy of Science under Grant JCTD-2021-10, in part by the National Natural Science Foundation of China under Grant 42104032 and Grant 42074042, and in part by the Pandeng Program of NSSC, CAS. *(Corresponding author: Xianyi Wang.)*

Tongsheng Qiu, Xianyi Wang, Feixiong Huang, Junming Xia, Fu Li, Zhuoyan Wang, Yueqiang Sun, Qifei Du, Weihua Bai, Yuerong Cai, Dongwei Wang, Yusen Tian, and Shuangshuang Cheng are with the Beijing Key Laboratory of Space Environment Exploration, National Space Science Center, Chinese Academy of Sciences, Beijing 100190, China (e-mail: qiutongsheng16@mails.ucas.ac.cn; wxy@nssc.ac.cn; huangfeixiong@nssc.ac.cn; xiajunming@nssc.ac.cn; lifu@nssc.ac.cn; wangzhuoyan@nssc.ac.cn; syq@nssc.ac.cn; dqf@nssc.ac.cn; baiweihua@nssc.ac.cn; cyr@nssc.ac.cn; wangdongwei@nssc.ac.cn; tianyusen@nssc.ac.cn; chengshuangshuang@nssc.ac.cn).

Qi Zheng is with the Shanghai ASES Spaceflight Technology, Company Ltd., Shanghai 201108, China (e-mail: zhengqi@asesspace.com).

Digital Object Identifier 10.1109/JSTARS.2023.3344762

I. Introduction

THE global navigation satellite system (GNSS) signals scattered off the Earth's surface can be taken as signals of opportunity for the Earth's remote sensing [1], and the GNSS-reflectometry (GNSS-R) receiver based on the bistatic radar scattering model is dedicated to receiving and processing GNSS reflected signals so as to generate basic measurements. To date, there have been more than 100 GNSS satellites from multiple different GNSS constellations, including the U.S. global positioning system (GPS), Russian GLONASS, European Galileo (GAL), Chinese BeiDou navigation satellite system (BDS), Japanese quasi-zenith satellite system, and Indian regional navigation satellite system. These GNSS satellites together provide abundant, free, and globally distributed reflected opportunity signals for the GNSS-R observation. Based on basic measurements generated by the GNSS-R receiver, geophysical parameters, such as ocean surface wind speeds [2], sea surface height [3], land soil moisture [4], vegetation biomass [5], ice properties, and snow water equivalent [6], can be retrieved.

GNSS signals reflected off the ocean surface can be received and processed by the spaceborne GNSS-R receiver onboard the low Earth orbit (LEO) satellite to generate delay-Doppler maps (DDMs) so as to retrieve ocean surface wind speeds with unprecedented temporal resolution and spatial coverage under all precipitating conditions [7], which benefits numerical weather prediction in particular. As a result, the retrieval of ocean surface wind speeds by means of the spaceborne GNSS-R technique has attracted much attention. A series of satellite missions carrying a spaceborne GNSS-R receiver, including the U.K.-Disaster Monitoring Constellation [8], TechDemoSat-1 [9], Cyclone Global Navigation Satellite System (CYGNSS) [10], BuFeng-1 A/B [11], FSSCat [12], and FY-3E [13] were carried out successively. However, all of these spaceborne GNSS-R receivers collected DDMs in raw counts only, and the DDM calibration as well as the retrieval of ocean surface wind speeds were conducted on the ground, which led to not only a heavy burden on downloading a wealth of scientific data but also global data latency of several hours or even more due to the bottleneck

© 2023 The Authors. This work is licensed under a Creative Commons Attribution-NonCommercial-NoDerivatives 4.0 License. For more information, see https://creativecommons.org/licenses/by-nc-nd/4.0/

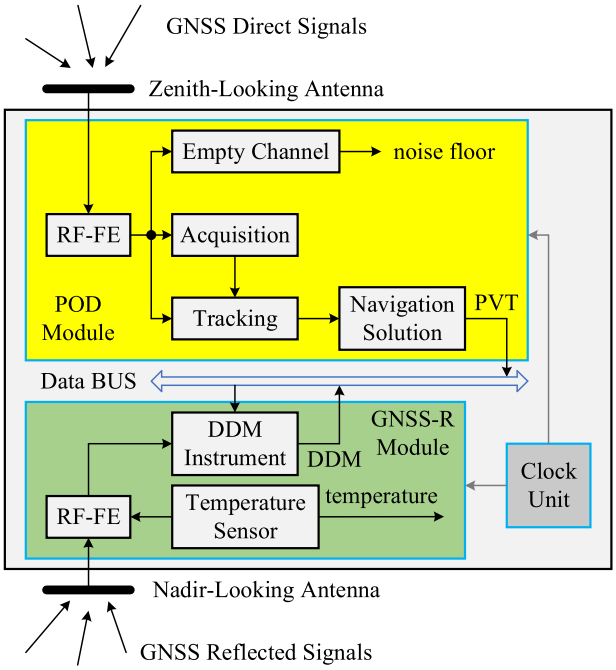

Fig. 1. One typical simplified system architecture of the spaceborne GNSS-R receiver. RF-FE denotes radio frequency front-end and PVT means position, velocity, and time data.

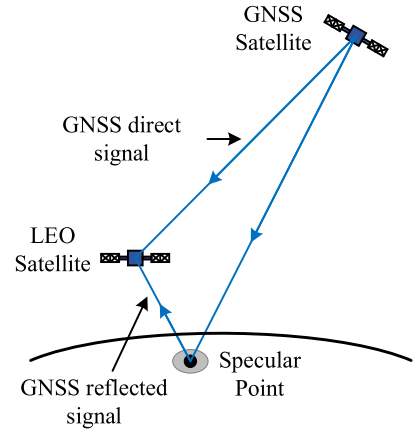

Fig. 2. One typical GNSS-R observation. The spaceborne GNSS-R receiver onboard the LEO satellite must simultaneously receive and process both direct and reflected signals from the same GNSS satellite, and there is an obvious power correlation between the direct and reflected signals with respect to the GNSS-R receiver.

in the satellite downlink. For example, China's FY-3E satellite has a global data latency of about 3 h [13]. In addition, a variety of maritime activities, such as marine fishing, marine transport, and marine scientific expeditions, all desire real-time oceanic weather information, of which the ocean surface wind speed is an important part. Thus, retrieving ocean surface wind speeds in real time on spaceborne GNSS-R receivers is of positive significance, but there has been no one who has proposed any algorithm for it, and therefore, we turned our focus to it [14].

As Fig. 1 shows, the spaceborne GNSS-R receiver is generally composed of one precise orbit determination (POD) module and one GNSS-R module [15]. The POD module corresponds to at least one zenith-looking antenna, and therefore, it processes GNSS direct signals to provide position, velocity, and time (PVT) information about the LEO satellite, GNSS satellites, and specular points. Moreover, GNSS direct signal processing in the POD module mainly includes signal acquisition and tracking. The signal tracking is usually by means of a combination of one phase-locked loop (PLL) and one delay-locked loop (DLL), and the PLL continuously outputs complex coherent integration results that contain both the carrier phase and power of the input GNSS direct signal. In addition, one empty channel in the POD module is specially designed to measure the real-time noise floor at the direct signal. More detailed information about the POD module can be found in the literature [16]. The GNSS-R module corresponds to at least one nadir-looking antenna, and therefore, it processes GNSS reflected signals to generate DDMs in raw counts. Utilizing the PVT information from the POD module, the GNSS-R module first estimates the whole path length and the Doppler shift of the GNSS reflected signal, and then generates a local replica to correlate with the input GNSS reflected signal. More detailed information about the GNSS-R module can be found in the literature [17]. In summary, the spaceborne GNSS-R receiver onboard the LEO satellite must simultaneously process both direct and reflected signals from the same GNSS satellite and there is an obvious power correlation between the direct and reflected signals with respect to the GNSS-R receiver, as shown in Fig. 2.

As a result, this article, for the first time, proposes an algorithm applied to the spaceborne GNSS-R receiver to retrieve ocean surface wind speeds in real time. This algorithm calibrates the GNSS direct signal power first, and then it estimates the real-time GNSS transmitter effective isotropic radiated power (EIRP) at the reflected signal according to the normalized antenna pattern of the corresponding GNSS satellite. After the DDM in raw counts has been converted to the DDM power in watts, the DDM bistatic radar cross section (BRCS) is derived further using the estimated real-time EIRP at the reflected signal, and then the DDM average (DDMA) and leading-edge slope (LES) are computed utilizing the predefined effective scattering area (ESA). Finally, the ocean surface wind speed is computed by means of pretrained both geophysical model functions (GMFs) and minimum variance (MV) coefficients [18].

The FY-3E satellite launched on 5 July 2021 is China's fifth polar-orbiting meteorology satellite and is in a sun-synchronous orbit at an altitude of 836 km and an inclination of 98.5°. The GNOS-II onboard China's FY-3E satellite was the first spaceborne integrated GNSS remote sensor around the world because it was first designed to combine one POD module, one GNSS radio occultation module, and one GNSS-R module together to monitor the ionosphere, neutral atmosphere, ocean, ice, and land at the same time, which is of great significance for the Earth remote sensing [15]. The GNOS-II is capable of receiving and processing both direct and reflected GPS L1 C/A, BDS B1I, and GAL E1B signals. Exploiting the scientific data from the GNOS-II, the proposed algorithm is validated carefully. Since BDS medium Earth orbit (MEO) satellites differ from BDS inclined geosynchronous orbit satellites in terms of orbital

altitude and transmitting power, only BDS B1I signals from BDS MEO satellites are adopted in this article.

The rest of this article is organized as follows. Section II introduces the proposed algorithm in detail. Exploiting the scientific data from the GNOS-II, this algorithm is validated carefully in Section III. Section IV gives some discussions, and some conclusions are drawn in Section V.

II. Algorithm

A. GNSS Direct Signal Power Calibration

The POD module in the spaceborne GNSS-R receiver usually conducts GNSS direct signal tracking by means of a combination of one PLL and one DLL. Each combination once tracks one GNSS direct signal only and the PLL continuously outputs complex coherent integration results with an output rate of the reciprocal of the coherent integration time. For example, in terms of GPS L1 C/A signal, the coherent integration time is usually configured as 20 ms to avoid the bit transition and to maintain an appropriate dynamic range for the PLL. In addition, these sequential complex coherent integration results contain both the carrier phase and power of the input GNSS direct signal, and therefore, modular squaring values (MSVs) of these sequential complex coherent integration results represent a series of power estimates in raw counts of the input GNSS direct signal when the PLL stays in a steady state.

In terms of GNSS direct signal power calibration, each MSV in raw counts is converted into the GNSS direct signal power in watts using the total POD module gain G_{POD}

$$Y_d = G_{\text{POD}}\ (T_{\text{POD}}) \cdot (C_d - \eta_d) \tag{1}$$

where C_d is the MSV in raw counts; η_d is the noise floor measured by the empty channel in the POD module; T_{POD} is the temperature of the radio-frequency front-end (RF-FE) in the POD module, and Y_d is the GNSS direct signal power. The total POD module gain G_{POD} is related to the temperature T_{POD}, and the relationship between G_{POD} and T_{POD} can be measured by a prelaunch thermal cycling test and saved as a lookup table (LUT). During an in-orbit operation phase, the temperature T_{POD} can be measured by a temperature sensor and then the total POD module gain G_{POD} can be computed by the LUT.

According to the electromagnetic wave propagation equation, GNSS transmitter EIRP at the GNSS direct signal is derived as

$$P_t\, G_{t,d} = Y_d \cdot \left(\frac{\lambda^2 G_d}{(4\pi R_d)^2} \right)^{-1} \tag{2}$$

where $P_t G_{t,d}$ is the GNSS transmitter EIRP at the GNSS direct signal; R_d is the distance from the GNSS satellite to the LEO satellite; λ is the wavelength of the GNSS signal; and G_d is zenith-looking antenna gain at the GNSS direct signal. The zenith-looking antenna pattern is calibrated in a microwave anechoic chamber by a prelaunch test and saved as an LUT. Utilizing the real-time PVT information from the POD module about LEO and GNSS satellites, R_d and elevation and azimuth angles of the GNSS satellite with respect to the zenith-looking antenna can be computed. Furthermore, mapping the computed elevation and azimuth angles to the zenith-looking antenna pattern LUT G_d can be determined.

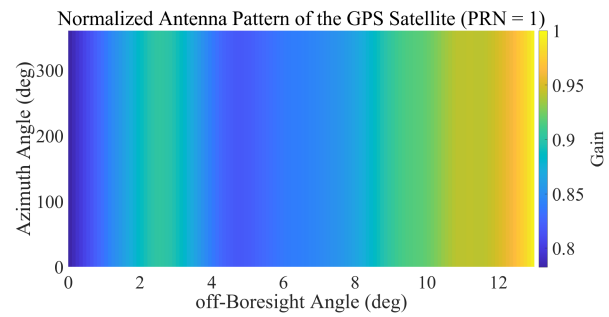

Fig. 3. One normalized antenna pattern of the GPS satellite (PRN = 1) on January 28, 2022. The normalized antenna pattern mainly varies with the off-boresight angle.

B. Calculating EIRP at the Reflected Signal

During the retrieval of ocean surface wind speeds, the GNSS transmitter EIRP at the reflected signal plays a key role in converting the DDM power in watts to the DDM BRCS. Since the transmitting power of GNSS satellites may change abruptly, the GNSS transmitter EIRP at the reflected signal is somewhat uncertain [19]. In general, the GNSS transmitter EIRP at the reflected signal is continuously estimated by ground power monitors [13]. As far as retrieving ocean surface wind speeds in real time on spaceborne GNSS-R receivers, it is necessary to measure the real-time GNSS transmitter EIRP at the reflected signal.

Fig. 2 shows that there is an obvious power correlation between direct and reflected signals from the same GNSS satellite under the GNSS-R observation. Moreover, antenna patterns of GNSS satellites are fixed after launching. Thus, according to normalized antenna patterns of GNSS satellites and the previously measured real-time GNSS transmitter EIRP at the direct signal, it is feasible for spaceborne GNSS receivers to compute the real-time GNSS transmitter EIRP at the reflected signal.

Based on GNSS transmitter EIRPs described in [13], one normalized antenna pattern of the GPS satellite (PRN = 1) is derived. As Fig. 3 shows, the normalized antenna pattern mainly varies with the off-boresight angle. As a result, only one row data along the off-boresight angle in each normalized antenna pattern needs to be saved as an LUT.

As Fig. 4 shows, based on the Earth-centered Earth-fixed (ECEF) frame, the off-boresight angle at the GNSS direct signal is given by

$$\theta_d = \operatorname{acos}\left(\frac{\left(-\vec{\boldsymbol{P}}_{\text{GNSS}}\right)\left(\vec{\boldsymbol{P}}_{\text{LEO}} - \vec{\boldsymbol{P}}_{\text{GNSS}}\right)}{\left|\vec{\boldsymbol{P}}_{\text{GNSS}}\right|\left|\vec{\boldsymbol{P}}_{\text{LEO}} - \vec{\boldsymbol{P}}_{\text{GNSS}}\right|} \right) \tag{3}$$

where θ_d is the off-boresight angle at the GNSS direct signal; $\operatorname{acos}(\cdot)$ is the inverse cosine function; $\vec{\boldsymbol{P}}_{\text{GNSS}}$ and $\vec{\boldsymbol{P}}_{\text{LEO}}$ are position vectors of the GNSS satellite and the LEO satellite, respectively. Utilizing the real-time PVT information from the POD module about LEO and GNSS satellites, $\vec{\boldsymbol{P}}_{\text{GNSS}}$ and $\vec{\boldsymbol{P}}_{\text{LEO}}$ can be, respectively, computed in orbit.

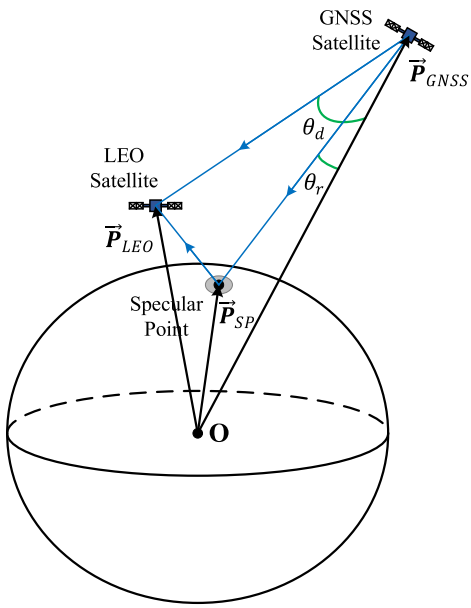

Fig. 4. One typical GNSS-R observation based on the ECEF frame. $\vec{P}_{\text{GNSS}}$, $\vec{P}_{\text{LEO}}$, and $\vec{P}_{\text{SP}}$ are position vectors of the GNSS satellite, the LEO satellite, and the specular point, respectively.

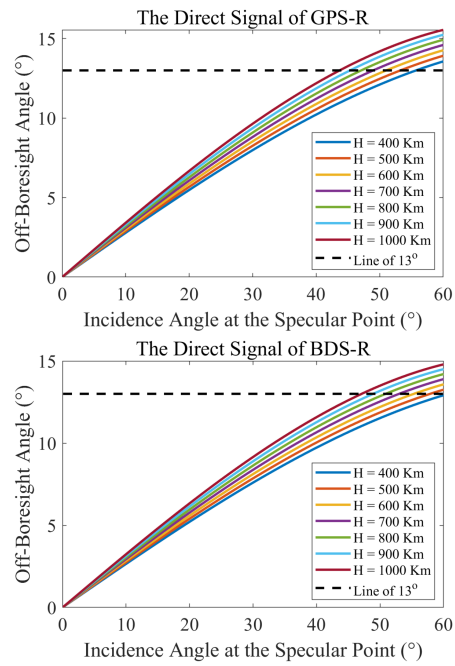

Fig. 5. Plots of off-boresight angles at the direct signal for GPS-R and BDS-R, respectively. The off-boresight angle at the direct signal is positively proportional to both the incidence angle at the specular point and the orbital height of the LEO satellite H. There are numbers of GNSS-R observations with an off-boresight angle greater than 13° at the direct signal.

Meanwhile, the off-boresight angle at the GNSS reflected signal from the same GNSS satellite is given by

$$\theta_r = \text{acos}\left(\frac{\left(-\vec{P}_{\text{GNSS}}\right)\left(\vec{P}_{\text{SP}} - \vec{P}_{\text{GNSS}}\right)}{\left|\vec{P}_{\text{GNSS}}\right|\left|\vec{P}_{\text{SP}} - \vec{P}_{\text{GNSS}}\right|}\right) \tag{4}$$

where θ_r is the off-boresight angle at the GNSS reflected signal and $\vec{P}_{\text{SP}}$ is the position vector of the predicted specular point. Utilizing the real-time PVT information from the POD module about LEO and GNSS satellites, the specular point position can be accurately estimated in orbit by the prediction algorithm [20].

According to (3) and (4), the GNSS transmitter EIRP at the reflected signal is derived as

$$P_t\, G_{t,r} = P_t\, G_{t,d} \cdot \frac{\overline{G_t}\,(\theta_r)}{\overline{G_t}\,(\theta_d)} \tag{5}$$

where $P_t G_{t,r}$ is the GNSS transmitter EIRP at the reflected signal and $\overline{G_t}$ represents the normalized antenna pattern of the corresponding GNSS satellite.

C. Obtaining Space-Measured GNSS Transmitter EIRPs

To obtain normalized antenna patterns of GNSS satellites, GNSS transmitter EIRPs over the entire off-boresight angle range should be measured first. At present, GNSS transmitter EIRPs are generally measured by ground power monitors [13], but ground-measured GNSS transmitter EIRPs are limited by a maximum off-boresight angle of 13° due to the Earth's curvature and local landforms. Hence, normalized antenna patterns of GNSS satellites derived from ground-measured GNSS transmitter EIRPs are also limited by a maximum off-boresight angle of 13°. However, as Fig. 5 shows, the off-boresight angle at the direct signal is positively proportional to both the incidence angle at the specular point and the orbital height of the LEO satellite, and there are numbers of GNSS-R observations with an off-boresight angle greater than 13° at the direct signal. Thus, if normalized antenna patterns of GNSS satellites derived from ground-measured GNSS transmitter EIRPs are used for computing the GNSS transmitter EIRP at the reflected signal, a number of GNSS-R observations with an off-boresight angle greater than 13° at the direct signal will be despondently deserted.

Since BDS satellites have higher orbital heights than GPS satellites, BDS satellites have smaller off-boresight angles at the direct signal than GPS satellites, with respect to the same LEO satellite and the same incidence angle at the specular point. Thus, as far as the proportion of GNSS-R observations with an off-boresight angle greater than 13° at the direct signal, BDS-R is lower than GPS-R. For example, in terms of the GNOS-II, the number of GNSS-R observations with an off-boresight angle greater than 13° at the direct signal accounts for 8.79% and 2.26% of the total number of GNSS-R observations for GPS-R and BDS-R, respectively, during August 1–10, 2022.

To make use of GNSS-R observations with an off-boresight angle greater than 13° at the direct signal, it is necessary for spaceborne GNSS-R receivers to measure GNSS transmitter EIRPs in orbit, namely that of obtaining space-measured GNSS transmitter EIRPs. Based on (1)–(3), spaceborne GNSS-R receivers can measure GNSS transmitter EIRPs at different off-boresight angles by continuously tracking all GNSS satellites within the field of view. Fig. 6 shows the flowchart of the algorithm proposed in this article to measure GNSS transmitter EIRPs in orbit. Normalized antenna patterns of GNSS satellites

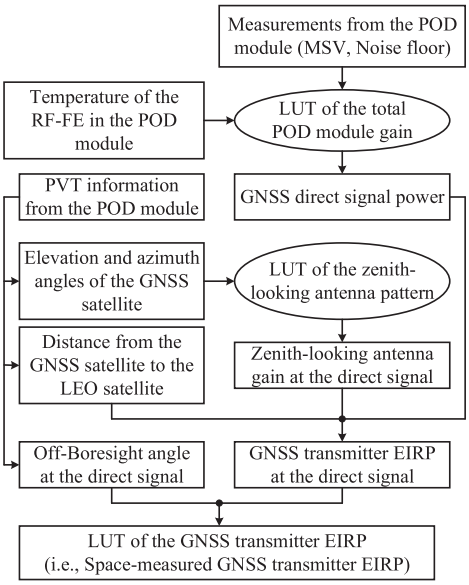

Fig. 6. Flowchart of the algorithm proposed in this article to measure the GNSS transmitter EIRP in orbit over the entire off-boresight angle range, namely that of obtaining the space-measured GNSS transmitter EIRP. The POD module is the precise orbit determination module. The RF-FE denotes radio frequency front-end, and PVT information about LEO and GNSS satellites means position, velocity, and time data.

derived from space-measured GNSS transmitter EIRPs are no longer limited by a maximum off-boresight angle of 13°.

D. DDM Calibration

To date, the basic measurement of the GNSS-R module in the spaceborne GNSS-R receiver is the DDM in raw counts. In terms of the DDM calibration, each DDM in raw counts is first converted into the DDM power in watts using the total GNSS-R module gain $G_{\text{GNSS-R}}$ [13]:

$$Y_r\ (\tau, f) = G_{\text{GNSS-R}}\ (T_{\text{GNSS-R}}) \cdot (C_r\,(\tau, f) - \eta_r) \tag{6}$$

where $C_r(\tau, f)$ is the DDM in raw counts; η_r is the DDM noise floor calculated by averaging over the DDM region where GNSS reflected signal power is not present; $T_{\text{GNSS-R}}$ is the temperature of the RF-FE in the GNSS-R module; $Y_r(\tau, f)$ is the DDM power in watts; τ and f are the time delay and Doppler frequency, respectively. The total GNSS-R module gain $G_{\text{GNSS-R}}$is related to the temperature $T_{\text{GNSS-R}}$. The relationship between $G_{\text{GNSS-R}}$ and $T_{\text{GNSS-R}}$ can be measured by a prelaunch thermal cycling test and saved as an LUT. During the in-orbit operation phase, the temperature $T_{\text{GNSS-R}}$ can be measured by a temperature sensor, and then the total GNSS-R module gain $G_{\text{GNSS-R}}$ can be computed by the LUT.

According to the bistatic radar equation, the DDM power in watts is converted to the DDM BRCS in square meters as [21]

$$\begin{aligned}\sigma\ (\tau, f) &= \sigma_0\ (\tau, f) \cdot A\,(\tau, f)\\ &= Y_r\ (\tau, f) \cdot \left(\frac{\lambda^2\,(P_t G_{t,r})\,G_r}{(4\pi)^3 R_t^2 R_r^2}\right)^{-1}\\ &= Y_r\ (\tau, f) \cdot G_{\text{BRCS}}^{-1}\end{aligned} \tag{7}$$

where $\sigma(\tau, f)$, $\sigma_0(\tau, f)$, and $A(\tau, f)$ are the BRCS, normalized BRCS (NBRCS), and ESA at the time delay τ and the Doppler frequency f, respectively; G_r is the nadir-looking antenna gain at the specular point; R_t and R_r are distances from the specular point to the transmitter and receiver, respectively; G_{BRCS} is the DDM BRCS gain that is a factor used for calculating DDM BRCSs. The nadir-looking antenna pattern is calibrated in microwave anechoic chamber by a prelaunch test and saved as an LUT. Utilizing the real-time PVT information from the POD module about both LEO and GNSS satellites and specular points, R_t and R_r can be computed, and elevation and azimuth angles of the specular point with respect to the nadir-looking antenna can be computed too. Furthermore, mapping the computed elevation and azimuth angles to the nadir-looking antenna pattern LUT, G_r can be determined.

The ESA at each time delay and Doppler frequency is a surface integration weighted by the Woodward ambiguity function (WAF) [21], [22]

$$A\ (\tau, f) = \iint_{\tilde{A}} \Lambda^2\,(\tau, x, y)\,|S\,(f, x, y)|^2 dxdy \tag{8}$$

where $\Lambda^2(\tau, x, y)|S(f, x, y)|^2$ is the WAF at the given time delay, Doppler frequency, and location on the sea surface; $\tilde{A}$ is the integration area defined by the WAF and the delay-Doppler coordinate. Based on predetermined orbital parameters of the LEO satellite and WAFs of GNSS reflected signals, the ESA, $A(\tau, f)$ can be computed under various incidence angles at the specular point and saved as an LUT.

E. Retrieving Ocean Surface Wind Speeds

The basic measurements for the retrieval of ocean surface wind speeds under diffuse scattering are DDMA and LES. The DDMA is calculated by averaging the DDM BRCS, and the LES is calculated as the slope of the leading edge of the integrated delay waveform (IDW) obtained by incoherently integrating the DDM BRCS elements along the Doppler frequency dimension [21]. In addition, DDMA and LES are computed over the same delay-Doppler window around the specular point to maintain consistency in spatial resolution [2], [23].

To reduce the size of the ESA LUT and simplify calculations on the DDMA, the DDMA is calculated as [7]

$$\overline{\sigma_0} = \frac{\bar{\sigma}}{\bar{A}} = \frac{\sum_{i=1}^{N}\sum_{j=1}^{M}\sigma\,(\tau_i, f_j)}{\sum_{i=1}^{N}\sum_{j=1}^{M}A\,(\tau_i, f_j)} \tag{9}$$

where $\overline{\sigma_0}$ is the DDMA; N and M represent the number of delay bins and Doppler bins in the delay-Doppler window around the specular point, respectively, which is mainly determined by the tradeoff between the spatial resolution and the signal-to-noise ratio (SNR).

To avoid complex fitting and interpolation calculations, the LES is calculated as

$$\begin{cases} s = \frac{\sum_{i=1}^{3}\omega_i(I(\tau_{k+2-i}) - I(\tau_{k+1-i}))}{\Delta\tau \cdot A(\tau_k, f_l)} \\ I\,(\tau_k) = \sum_{j=1}^{M}\sigma\,(\tau_k, f_j) \\ \Delta\tau = \tau_k\ - \tau_{k-1} \end{cases} \tag{10}$$

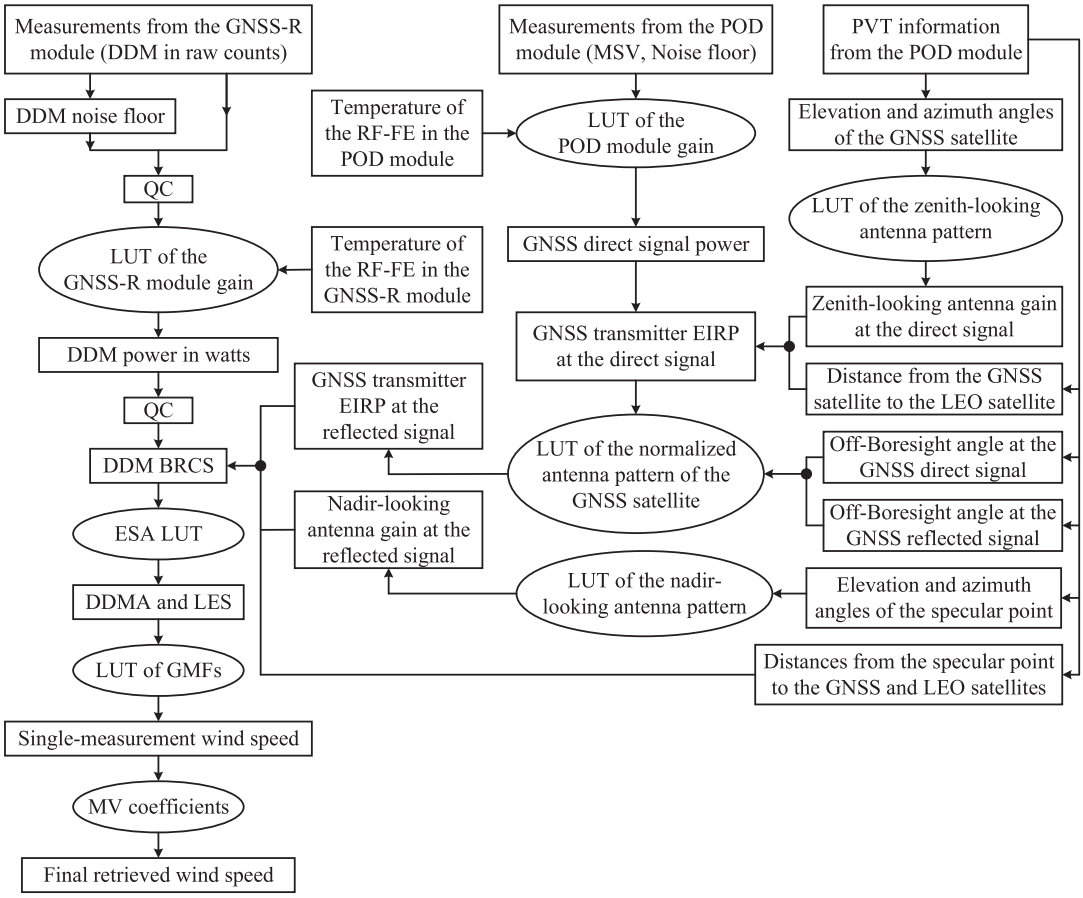

Fig. 7. Flowchart of the proposed algorithm applied to spaceborne GNSS-R receivers to retrieve ocean surface wind speeds in real time. All basic measurements and necessary parameters can be directly collected or computed in orbit.

where s is the LES; ω_i is the ith positive empirical weight and $\omega_1 + \omega_2 + \omega_3 = 1$; $I(\tau_k)$ is the kth sample of the IDW; τ_k and f_l are time delay and Doppler frequency at the specular point, respectively, and $\Delta\tau$ is the delay resolution of the DDM. According to (9) and (10), only $\bar{A}$ and $A(\tau_k, f_l)$ need to be saved into the ESA LUT.

DDMAs are converted to wind speeds using the DDMA GMF LUT, and LESs are converted to wind speeds too by using the LES GMF LUT. The DDMA and LES GMFs are all obtained by ground training and saved as LUTs, which are based on a large training dataset containing enough measurements. Finally, the final retrieved wind speeds are computed by combining wind speeds retrieved from the DDMA and the LES by means of an MV estimator [21].

It is worth noting that quality control (QC) is an essential step to filter out bad values and unsatisfactory measurements, which contributes to improving retrieval precision. Thus, the QC should be implemented in real time. Moreover, the QC can be performed on any variable concerned with the retrieval algorithm, such as SNR and noise floor of the DDM.

All in all, the flowchart of the algorithm proposed in this article is shown in Fig. 7. Observing the whole flow of the proposed algorithm, only the DDM region corresponding to the delay-Doppler window needs to be calibrated and then used to compute DDMA and LES, and therefore elsewhere in each DDM can be deserted after the DDM noise floor has been computed, which significantly lightens the computation burden in orbit.

III. Validation

A. FY-3E GNOS-II Data

The GNOS-II onboard China's FY-3E satellite has two zenith-looking antennas and one nadir-looking antenna, and it is capable of receiving and processing direct and reflected GPS L1 C/A, BDS B1I, and GAL E1B signals. Moreover, the GNOS-II has eight DDM channels with a DDM output rate of 1 Hz, and therefore, it is able to generate at most eight DDMs per second. The coherent integration time is 1 ms, and the total integration time is 1000 ms. The DDM generated by the GNOS-II is nonuniform and has 122 time delays times 20 Doppler frequencies. As Fig. 8 shows, the delay resolution is 0.125 chips from -2.875 to 2.875 chips and 0.25 chips elsewhere in the range from -12.25 to 12.125 chips, and the Doppler frequency resolution is 500 Hz from -5000 to 4500 Hz. Both the delay and the Doppler frequency are relative to the specular point.

Since the DDM output rate is 1 Hz, all types of level-1 (L1) scientific data from the GNOS-II released by the Chinese National Satellite Meteorological Center (NSMC) have a data rate of 1 Hz to maintain a consistency. In terms of time-varying variables, such as positions of the receiver and transmitters, their values

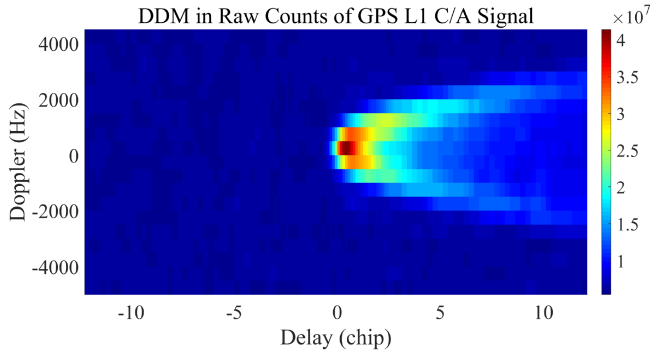

Fig. 8. Example of one GPS-R DDM in raw counts generated by the GNOS-II onboard China's FY-3E satellite.

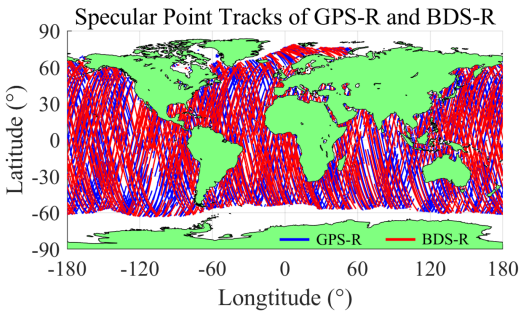

Fig. 9. Specular points corresponding to both GPS-R and BDS-R from the GNOS-II onboard China's FY-3E satellite during August 1–10, 2022. The specular points almost cover global oceans.

per second contained in L1 scientific datasets are their transient values at the middle moment in each second when generating DDMs. Based on L1 scientific datasets from the GNOS-II, the retrieval of global ocean surface wind speeds was conducted by ground data-processing centers [19], [22], [24], and retrieved global ocean surface wind speeds have been released by the NSMC as one of primary products of the GNOS-II, which indicates that the data quality of L1 scientific datasets from the GNOS-II meets the requirement of operational use.

In this article, the proposed algorithm is analyzed and validated using ten-day L1 scientific data from the GNOS-II over the ocean, during August 1–10, 2022. Half of the L1 scientific data with odd ordinals is taken as the training dataset to train GMFs and MV coefficients, and the other half with even ordinals is taken as the testing dataset for validation. Fig. 9 shows that specular points corresponding to both GPS-R and BDS-R from the GNOS-II, during August 1–10, 2022, almost cover global oceans.

B. Estimating GNSS Direct Signal Power

In the design phase of the GNOS-II, researchers did not consider retrieving ocean surface wind speeds in real time on spaceborne GNSS-R receivers. As a result, there was no temperature sensor integrated into the RF-FE in the POD module of the GNOS-II, so there was no LUT storing the total POD module gain. Thankfully, both the noise floor at the direct signal and the direct SNR are provided by the L1 scientific dataset from the GNOS-II. Facing with this condition, the estimate of the GNSS direct signal power in this validation is derived as

$$\begin{cases} Y_d = G_{\text{POD}} \cdot (\text{SNR}_d \cdot \eta_d) \\ \text{SNR}_d = \frac{C_d - \eta_d}{\eta_d} \end{cases} \tag{11}$$

where Y_d is the estimate of the GNSS direct signal power; SNR_d is the direct signal to noise ratio; η_d is the noise floor at the direct signal. G_{POD} is the total POD module gain, and it is set to an empirical constant to make the value of Y_d within a reasonable range in this validation.

TABLE I
BOTH THE NUMBER AND THE DATA RATE OF REMAINING GPS-R AND BDS-R MEASUREMENTS AFTER QC

Datasets \ Values	GPS-R measurements		BDS-R measurements	
	Num	Rate	Num	Rate
Training Dataset	106302	20.81%	81114	20.35%
Testing Dataset	106302		81114	
Total	212604	41.61%	162228	40.70%

C. Quality Control

Similarly, there are no space-measured GNSS transmitter EIRPs from the GNOS-II, and therefore, normalized antenna patterns of GNSS satellites in this validation are derived from ground-measured GNSS transmitter EIRPs described in [13], and therefore, all GNSS-R observations with an off-boresight angle greater than 13° at the direct signal are despondently deserted. What is more, this article empirically chose −2 dB as the threshold of the SNR at the specular point for the QC, and therefore, any DDM whose SNR at the specular point is not greater than −2 dB is discarded. The SNR at the specular point is calculated as

$$\text{SNR}_{\text{SP}} = \frac{C_r(\tau_k, f_l) - \eta_r}{\eta_r} \tag{12}$$

where SNR_{SP} is the SNR at the specular point, and $C_r(\tau_k, f_l)$ is the DDM element corresponding to the specular point. After QC, both the number and the data rate of remaining GPS-R and BDS-R measurements are given in Table I.

D. Comparing DDM BRCS Gains

It is worth mentioning that the total POD module gain G_{POD} is not a constant in actual and related to the temperature of the RF-FE in the POD module, and therefore, setting G_{POD} as an empirical constant undoubtedly brings an error to the estimate of the GNSS direct signal power. According to (2) and (5), the estimate of the GNSS direct signal power is directly related to the estimated real-time GNSS transmitter EIRP at the reflected signal, and further has an effect on the DDM BRCS gain in (7). To evaluate the impact of the estimation error of the GNSS direct signal power on DDM BRCS gain, a comparison between the estimated G_{BRCS} and the ground-monitored G_{BRCS} is performed. The estimated G_{BRCS} is derived from (11) and the ground-monitored G_{BRCS} is derived by the ground data-processing center and provided by the scientific dataset from the GNOS-II. Based on the training dataset, Fig. 10 shows that the estimated G_{BRCS} has a high correlation and

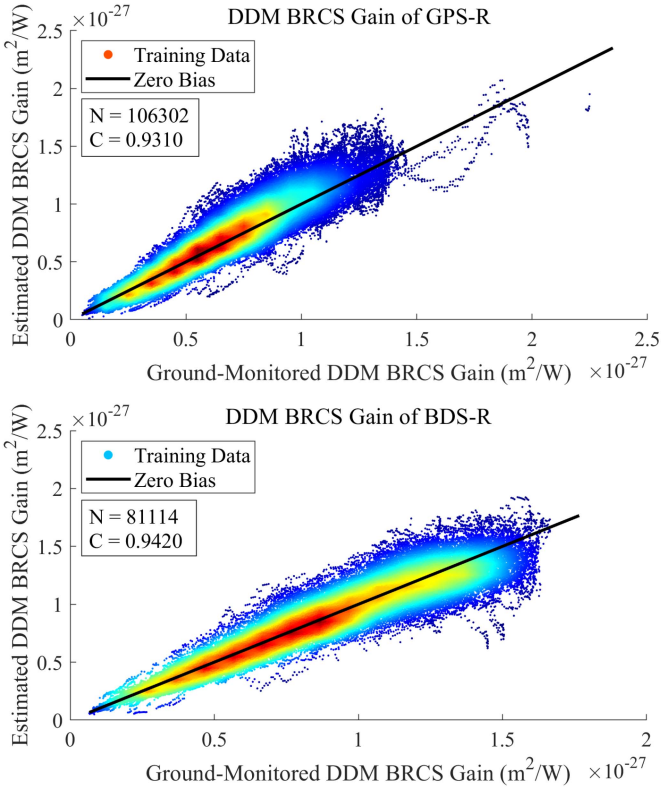

Fig. 10. Density scatter plots between estimated and ground-monitored DDM BRCS gains of GPS-R and BDS-R, respectively. N is the number of remaining measurements after the QC, and C is the overall correlation coefficient.

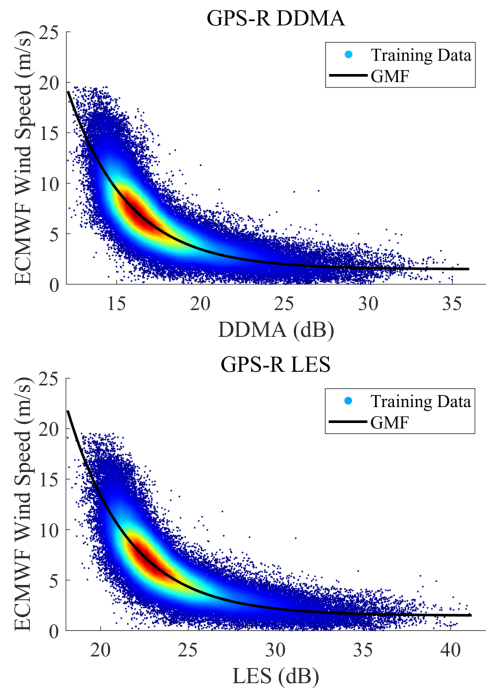

Fig. 11. Density scatter plots between basic measurements (DDMA and LES) and collocated ECMWF wind speeds for GPS-R.

consistency with the ground-monitored G_{BRCS}, and the overall correlation coefficients of GPS-R and BDS-R are 0.9310 and 0.9420, respectively. Certainly, based on the testing dataset, the estimated G_{BRCS} also has such a high correlation and consistency with the ground-monitored G_{BRCS}. Consequently, it is feasible that G_{POD} is set to an empirical constant to make the value of Y_d within a reasonable range in this validation.

E. Determining Delay-Doppler Window

Since the delay resolution is 0.125 chips over the DDM region around the specular point, the delay-Doppler window, over which DDMA and LES are computed, is a 5 time delay times 3 Doppler frequencies window limited by the 25 km spatial resolution [13]. As far as the (9), $N = 5$, and $M = 3$. Furthermore, the specular point is located in the center of the delay-Doppler window, and therefore, τ_3 and f_3 in (9) are time delay and Doppler frequency at the specular point, respectively.

F. Retrieving Ocean Surface Wind Speeds

To train and test both GMFs and MV coefficients, all measurements are collocated with the European Centre for Medium-Range Weather Forecasts (ECMWF) ERA5 reanalysis wind speeds using linear interpolation in time and space. The training dataset and collocated ECMWF wind speeds are used to train GMFs and MV coefficients, and then the testing dataset is used to perform ocean surface wind speed retrieval by obtained GMFs and MV coefficients. Finally, the retrieved ocean surface wind speeds are compared with collocated ECMWF wind speeds to calculate the overall root-mean-square error (RMSE), and the RMSE is generally used to evaluate the performance of the ocean surface wind speed retrieval algorithm.

As previously mentioned, this article empirically chose −2 dB as the threshold of the SNR at the specular point for the QC, and this threshold is high enough to filter out more than half of DDMs. As a result, almost all DDMs collected under high wind speeds (>20 m/s) are removed, which meets the requirement of retrieving medium to low ocean surface wind speeds in this validation. Consequently, an exponential function, in this article, is used for nonlinear least-square fitting to obtain final GMFs. Figs. 11 and 12 show the density scatter plots between basic measurements (DDMA and LES) and collocated ECMWF wind speeds for GPS-R and BDS-R, respectively. The GMFs match with the highest density part of the data.

Employing obtained GMFs, DDMAs and LESs derived from the testing dataset are converted to DDMA wind speeds and LES wind speeds, respectively. Subsequently, the final retrieved ocean surface wind speeds are calculated while combining the DDMA wind speed and the LES wind speed by obtained MV coefficients. Final retrieved ocean surface wind speeds are compared with the collocated ECMWF wind speeds. As Fig. 13 shows, the zero-bias lines match with the highest density part of the data, and the overall RMSEs of GPS-R and BDS-R are 1.68 m/s and 1.50 m/s, respectively.

IV. Discussions

The method applied to calibrate the DDM power, as (6) shows, has been adopted by the GNOS-II onboard China's FY-3E

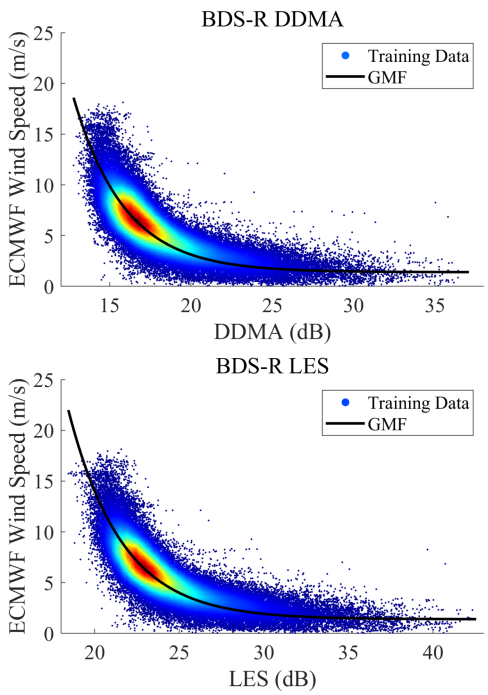

Fig. 12. Density scatter plots between basic measurements (DDMA and LES) and collocated ECMWF wind speeds for BDS-R.

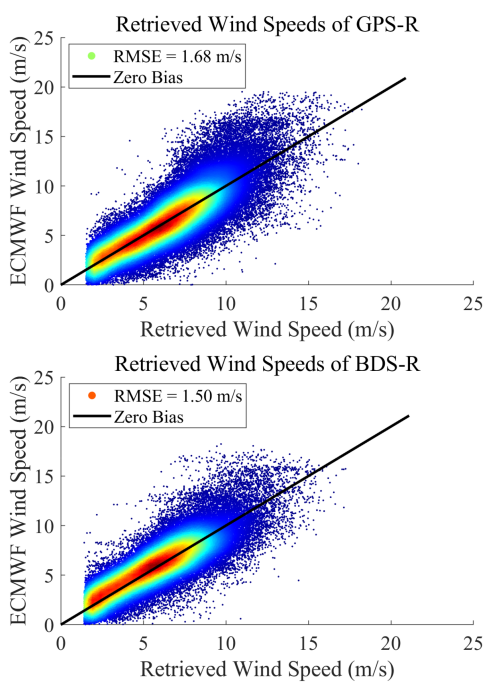

Fig. 13. Density scatter plots between final retrieved wind speeds and collocated ECMWF wind speeds for GPS-R and BDS-R, respectively.

satellite, and it has been proved to be effective. As (1) shows, the method applied to calibrate the GNSS direct signal power is similar to the method used to calibrate the DDM power. Based on authors' experience in designing the GNOS-II, we think that (1) is feasible.

The DDM in raw counts has lower output rate than other variables such as the estimated GNSS transmitter EIRP at the

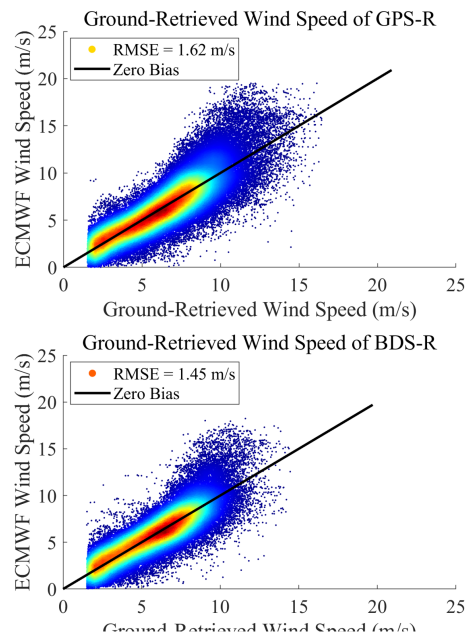

Fig. 14. Density scatter plots between final ground-retrieved wind speeds and collocated ECMWF wind speeds for GPS-R and BDS-R, respectively.

reflected signal. To maintain consistency in the final output rate among these variables, variables with a high original output rate can merely take and output their transient values at the middle moment or their averages over the duration of generating one DDM.

Utilizing the ground-monitored DDM BRCS gain and similar GMFs, ground-retrieved ocean surface wind speeds of GPS-R and BDS-R have overall RMSEs of 1.62 m/s and 1.45 m/s, respectively, as Fig. 14 shows. The ground-retrieved ocean surface wind speeds have lower overall RMSE than space-retrieved ocean surface wind speeds shown in Fig. 13 because the total POD module gain G_{POD} is set to an empirical constant in this validation and then undoubtedly brings an error to the estimate of the GNSS direct signal power. Since authors were responsible for designing the GNOS-II, conducting the DDM calibration, and performing the ground retrieval of ocean surface wind speeds, we do confirm that the overall RMSE of space-retrieved wind speeds will be competitive with that of ground-retrieved wind speeds if the temperature of the RF-FE in the POD module is measured in orbit and the relationship between the total POD module gain and the temperature of the RF-FE in the POD module is predefined by the prelaunch thermal cycling test.

Although the estimation error of the GNSS direct signal power in this validation leads to a descent in the overall RMSE of retrieved ocean surface wind speeds, this descent is slight. As Fig. 10 shows, the estimated DDM BRCS gain has a high correlation and consistency with the ground-monitored DDM BRCS gain. In addition, the final overall accuracy of retrieved ocean surface wind speeds, as Fig. 13 shows, is good and inspiring.

In the future, the algorithm will be implemented in upcoming spaceborne GNSS-R missions and then attract much attention to retrieving ocean surface wind speeds and other geophysical parameters in real time on spaceborne GNSS-R receivers.

V. Conclusion

This article, for the first time, proposed an algorithm for spaceborne GNSS-R receivers to retrieve ocean surface wind speeds in real time, which contributes to not only lightening the burden on downloading a wealth of scientific data but also broadcasting real-time ocean surface wind speeds to users. As far as for the proposed algorithm, there are no additional requirements of hardware resources for the real-time retrieval in terms of a general spaceborne GNSS-R receiver, except for integrating a temperature sensor on the RF-FE in the POD module. In addition, all basic measurements and key parameters can be directly collected in orbit, and complex computations such as DDM calibration and ocean surface wind speed retrieval can be conducted in orbit by a series of related LUTs. Based on a general spaceborne GNSS-R receiver, the added computations are only about 29 arithmetic operations and two-time commonly used inverse cosine operations in terms of the proposed algorithm, which consumes only a negligible amount of time. Although the DDM calibration and wind speed retrieval is similar to those used in CYGNSS and other spaceborne GNSS-R missions, how to handily conduct real-time calibration in orbit and without ground support is the key. The main innovation of the article is that a feasible method for in-orbit calculation of the real-time EIRP at the reflected signal in terms of methodology is proposed.

If normalized antenna patterns of GNSS satellites are derived from the off-the-shelf ground-measured GNSS transmitter EIRPs, all related LUTs will be prepared well on the ground before launching; otherwise, only space-measured GNSS transmitter EIRPs need to be obtained in orbit to generate normalized antenna patterns before conducting the retrieval of ocean surface wind speeds. Utilizing the L1 scientific dataset from the GNOS-II onboard China's FY-3E satellite, this proposed algorithm is carefully validated and discussed. The final results show that this proposed algorithm is feasible and able to achieve a competitive overall retrieval accuracy in comparison to the current retrieval algorithm used on the ground.

Since there is an obvious power correlation between the direct and reflected signals from the same GNSS satellite under the GNSS-R observation, the proposed algorithm calibrates the GNSS direct signal power first and then estimates the real-time GNSS transmitter EIRP at the reflected signal by normalized antenna patterns of GNSS satellites, which is no longer affected by the fluctuation of the transmitting power of GNSS satellites. The normalized antenna patterns of GNSS satellites derived from ground-measured GNSS transmitter EIRPs are limited by a maximum off-boresight angle of 13°, due to both the Earth's curvature and local landforms. However, there are a number of GNSS-R observations with an off-boresight angle greater than 13° at the direct signal, especially for GPS-R. To make use of GNSS-R observations with an off-boresight angle greater than 13° at the direct signal, it is necessary for spaceborne GNSS-R receivers to measure GNSS transmitter EIRPs in orbit. Consequently, an algorithm is proposed in this article for spaceborne GNSS-R receivers to obtain space-measured GNSS transmitter EIRPs from which normalized antenna patterns of GNSS satellites can be derived. What is more, the space-measured GNSS transmitter EIRPs are immune to multipath signals and terrestrial RF interference. On the other hand, since the off-boresight angle at the direct signal is positively proportional to the incidence angle at the specular point, reducing the observable range of the incidence angle is able to decrease the maximum value of the off-boresight angle at the direct signal to a value lower than 13°, and then normalized antenna patterns of GNSS satellites can be derived from the off-the-shelf ground-measured GNSS transmitter EIRPs, which avoids the process of obtaining space-measured GNSS transmitter EIRPs but leads to a descent on the number of GNSS-R observations.

According to validation results, it is feasible that the total POD module gain is set to an empirical constant to make the estimate of the GNSS direct signal power within a reasonable range, which significantly simplifies the engineering implementation of the proposed algorithm and merely brings about a slight descent on the overall RMSE of retrieved ocean surface wind speeds. Under this simplification, normalized antenna patterns of GNSS satellites must be derived from off-the-shelf ground-measured GNSS transmitter EIRPs with a cost of losing some GNSS-R observations with an off-boresight angle greater than 13°.

Acknowledgment

The authors would like to thank the National Satellite Meteorological Center, Chinese Meteorological Administration, for providing the GNOS-II data and the Copernicus Climate Change Service for providing the ECMWF ERA5 reanalysis data.

References

[1] V. U. Zavorotny, S. Gleason, E. Cardellach, and A. Camps, "Tutorial on remote sensing using GNSS bistatic radar of opportunity," *IEEE Geosci. Remote Sens. Mag.*, vol. 2, no. 4, pp. 8–45, Dec. 2014.

[2] M. P. Clarizia and C. S. Ruf, "Wind speed retrieval algorithm for the cyclone global navigation satellite system (CYGNSS) mission," *IEEE Trans. Geosci. Remote Sens.*, vol. 54, no. 8, pp. 4419–4432, Aug. 2016.

[3] W. Li, E. Cardellach, F. Fabra, S. Ribo, and A. Rius, "Assessment of spaceborne GNSS-R ocean altimetry performance using CYGNSS mission raw data," *IEEE Trans. Geosci. Remote Sens.*, vol. 58, no. 1, pp. 238–250, Jan. 2020.

[4] X. Wu, W. Ma, J. Xia, W. Bai, S. Jin, and A. Calabia, "Spaceborne GNSS-R soil moisture retrieval: Status, development opportunities, and challenges," *Remote Sens.*, vol. 13, no. 1, 2021, Art. no. 45.

[5] X. Wu, P. Guo, Y. Sun, H. Liang, X. Zhang, and W. Bai, "Recent progress on vegetation remote sensing using spaceborne GNSS-reflectometry," *Remote Sens.*, vol. 13, no. 21, 2021, Art. no. 4244.

[6] J. F. Munoz-Martin et al., "Snow and ice thickness retrievals using GNSS-R: Preliminary results of the MOSAiC experiment," *Remote Sens.*, vol. 12, no. 24, 2020, Art. no. 4038.

[7] *CYGNSS Handbook*, 1st ed. Ann Arbor, MI, USA: Univ. of Michigan, 2016.

[8] M. P. Clarizia, C. P. Gommenginger, S. T. Gleason, M. A. Srokosz, C. Galdi, and M. Di Bisceglie, "Analysis of GNSS-R delay-Doppler maps from the U.K.-DMC satellite over the ocean," *Geophysical Res. Lett.*, vol. 36, no. 2, 2009, Art. no. L02608.

[9] G. Foti et al., "Spaceborne GNSS reflectometry for ocean winds: First results from the U.K. TechDemoSat-1 mission," *Geophysical Res. Lett.*, vol. 42, no. 13, pp. 5435–5441, 2015.

[10] C. Ruf et al., "CYGNSS: Enabling the future of hurricane prediction," *IEEE Geosci. Remote Sens. Mag.*, vol. 1, no. 2, pp. 52–67, Jun. 2013.

[11] C. Jing, X. Niu, C. Duan, F. Lu, G. Di, and X. Yang, "Sea surface wind speed retrieval from the first Chinese GNSS-R mission: Technique and preliminary results," *Remote Sens.*, vol. 11, no. 24, 2019, Art. no. 3013.

[12] J. F. Munoz-Martin et al., "In-orbit validation of the FMPL-2 instruments-the GNSS-R and L-band microwave radiometer payload of the FSSCat mission," *Remote Sens.*, vol. 13, no. 1, 2021, Art. no. 121.

[13] G. Yang et al., "FY3E GNOS II GNSS reflectometry: Mission review and first results," *Remote Sens.*, vol. 14, no. 4, 2022, Art. no. 988.

[14] T. Qiu et al., "The recent advance in GRSA," in *Proc. IEEE Int. Geosci. Remote Sens. Symp.*, 2022, pp. 7651–7653.
[15] T. Qiu et al., "An innovative signal processing scheme for spaceborne integrated GNSS remote sensors," *Remote Sens.*, vol. 15, no. 3, 2023, Art. no. 745.
[16] B. Parkinson and J. Spilker, *Global Positioning System: Theory and Applications I*. Washington, DC, USA: American Institute of Aeronautics and Astronautics, 1996.
[17] S. Jin, E. Cardellach, and F. Xie, *GNSS Remote Sensing: Theory, Methods and Applications*. Dordrecht, The Netherlands: Springer 2014.
[18] M. P. Clarizia, C. S. Ruf, P. Jales, and C. Gommenginger, "Spaceborne GNSS-R minimum variance wind speed estimator," *IEEE Trans. Geosci. Remote Sens.*, vol. 52, no. 11, pp. 6829–6843, Nov. 2014.
[19] F. Huang et al., "Assessment of FY-3E GNOS-II GNSS-R global wind product," *IEEE J. Sel. Topics Appl. Earth Observ. Remote Sens.*, vol. 15, pp. 7899–7912, 2022.
[20] Y. Tian et al., "Improved specular point prediction precision using gradient descent algorithm," *Adv. Space Res.*, vol. 65, pp. 1568–1579, 2020.
[21] S. Gleason, C. S. Ruf, M. P. Clarizia, and A. J. O'Brien, "Calibration and unwrapping of the normalized scattering cross section for the cyclone global navigation satellite system," *IEEE Trans. Geosci. Remote Sens.*, vol. 54, no. 5, pp. 2495–2509, May 2016.
[22] F. Huang et al., "Characterization and calibration of spaceborne GNSS-R observations over the ocean from different BeiDou satellite types," *IEEE Trans. Geosci. Remote Sens.*, vol. 60, 2022, Art. no. 5804511.
[23] M. P. Clarizia and C. S. Ruf, "On the spatial resolution of GNSS reflectometry," *IEEE Geosci. Remote Sens. Lett.*, vol. 13, no. 8, pp. 1064–1068, Aug. 2016.
[24] F. Huang et al., "Spaceborne GNSS reflectometry with Galileo signals on FY-3E/GNOS-II: Measurements, calibration, and wind speed retrieval," *IEEE Geosci. Remote Sens. Lett.*, vol. 20, 2023, Art. no. 3501505.

Tongsheng Qiu received the B.S. degree in electronic information engineering from Xidian University, Xi'an, China, in 2016, and the Ph.D. degree in earth and space probing technology from the University of Chinese Academy of Sciences, Beijing, China, in 2021.

He is currently a Postdoctoral Researcher with the National Space Science Center, Chinese Academy of Sciences, Beijing, China. His research interests include GNSS signal processing, GNSS remote sensing technologies, and embedded system design and development.

Qi Zheng received the Ph.D. degree in electronic information from the School of Automation Science and Electrical Engineering from Beihang University, Beijing, China, in 2014.

In 2014, he joined the Shanghai Institute of Aerospace Systems Engineering as a Microsatellite Engineer. Since 2020, he has been the CTO of the Shanghai ASES Spaceflight Technology, Company Ltd. His current research interests include the overall design of microsatellites, advanced aerospace electronics, and space-based IoT technology.

Xianyi Wang received the B.S. degree in electronic information Engineering from the University of Science and Technology of China, Hefei, China, in 2004, and the M.S. and Ph.D. degrees in space physics from the University of Chinese Academy of Sciences, Beijing, China, in 2007 and 2012, respectively.

He is currently a Professor with the National Space Science Center, Chinese Academy of Sciences, Beijing, China. His research fields include GNSS remote sensing technologies and applications, GNSS signal processing, navigation, communication, and embedded system design and development.

Feixiong Huang received the B.S. degree in geodesy and geomatics engineering from Wuhan University, Wuhan, China, in 2014, and the Ph.D. degree in aeronautical and astronautical engineering from Purdue University, West Lafayette, IN, USA, in 2020.

He was a Visiting Scientist with the Royal Netherlands Meteorological Institute, DeBilt, The Netherlands, in summer 2019 under the EUMETSAT OSI SAF Visiting Scientist Program. He is currently a Postdoctoral Researcher with the National Space Science Center, Chinese Academy of Sciences, Beijing, China. His research fields include GNSS remote sensing applications, microwave ocean remote sensing, and atmospheric data assimilation.

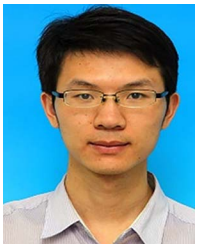

Junming Xia received the B.S. degree in physics from the Changsha University of Science and Technology, Changsha, China, in 2009, and the M.S. and Ph.D. degrees in earth and space probing technology from the University of Chinese Academy of Sciences, Beijing, China, in 2012 and 2015, respectively.

He is currently an Associate Professor with the National Space Science Center, Chinese Academy of Sciences, Beijing, China. His research fields include GNSS remote sensing applications, electromagnetic scattering models, and electromagnetic wave propagation.

Fu Li received the B.S. degree in automation from the Taiyuan University of Technology, Taiyuan, China, in 2014, and the M.S. degree in control science and engineering from Beihang University, Beijing, China, in 2017. He is currently working toward the Ph.D. degree in earth and space probing technology with the University of Chinese Academy of Sciences, Beijing, China.

His research fields include GNSS remote sensor design and evaluation.

Zhuoyan Wang received the B.S. degree in computer science and technology from the Huazhong University of Science and Technology, Wuhan, China, in 2018, and the M.S. degree in electronic and communication engineering from the University of Chinese Academy of Sciences, Beijing, China, in 2021.

He is currently an Engineer with the National Space Science Center, Chinese Academy of Sciences, Beijing, China. His research fields include GNSS remote sensor design and evaluation.

Yueqiang Sun received the B.S. degree in radio physics from Nanjing University, Nanjing, China, in 1985, and the M.S. and Ph.D. degrees in space physics from the University of Chinese Academy of Sciences, Beijing, China, in 1991 and 2002, respectively.

She is currently a Professor with the National Space Science Center, Chinese Academy of Sciences, Beijing, China. Her research fields include atmospheric physics, ionospheric physics, magnetic physics, space physics, GNSS remote sensing technologies and applications, GNSS remote sensor designs, and spaceborne spatial environment exploration technologies.

Qifei Du received the B.S. degree in information engineering from the Beijing Institute of Technology, Beijing, China, in 2002, the M.S. degree in electromagnetic fields and microwave technology from the Beijing Institute of Technology, Beijing, China, in 2004, and the Ph.D. degree in space physics from the University of Chinese Academy of Sciences, Beijing, China, in 2012.

He is currently a Professor with the National Space Science Center, Chinese Academy of Sciences, Beijing, China. His research fields include GNSS remote sensing technologies and GNSS remote sensor design, and he has been the Principal Investigator of the occultation payloads for Yinghuo Satellite and FY-3 satellites.

Weihua Bai received the B.S. degree in electronic science and technology from Inner Mongolia University, Huhehaote, China, in 2003, and the Ph.D. degree in space physics from the University of Chinese Academy of Sciences, Beijing, China, in 2008.

He is currently a Professor with the National Space Science Center, Chinese Academy of Sciences, Beijing, China. His research interest focuses on GNSS remote sensing applications.

Yuerong Cai received the B.S. degree in physics education from Shaoyang University, Shaoyang, China, in 2000, the M.S. degree in particle physics and nuclear physics from Sichuan University, Chengdu, China, in 2006, and the Ph.D. degree in space physics from University of Chinese Academy of Sciences, Beijing, China, in 2017.

He is currently an Associate Professor with the National Space Science Center, Chinese Academy of Sciences, Beijing, China. His research fields include complex high-speed digital circuit design and radiation hardening.

Dongwei Wang received the Ph.D. degree in earth and space probing technology from the University of Chinese Academy of Sciences, Beijing, China, in 2021.

He is currently an Associate Professor with the National Space Science Center, Chinese Academy of Sciences, Beijing, China. His research fields include GNSS remote sensing technologies and embedded system design and development.

Yusen Tian received the Ph.D. degree in earth and space probing technology from the University of Chinese Academy of Sciences, Beijing, China, in 2021.

He is currently working with the National Space Science Center, Chinese Academy of Sciences, Beijing, China. His research interest focuses on GNSS-based remote sensing.

Shuangshuang Cheng received the B.S. and M.S. degrees in measurement and control technology and instrumentation from the China University of Geosciences, Beijing, China, in 2016 and 2019, respectively.

She is currently an Engineer with the National Space Science Center, Chinese Academy of Science, Beijing, China. Her research fields include testing, software development, and graphical interface development.